PAPER

Fabrication of suspended, three-dimensional chiral plasmonic nanostructures with single-step electron-beam lithography

Eunice Sok Ping Leong,*[a] Jie Deng,[a] Eng Huat Khoo,[b] Siji Wu,[a] Wee Kee Phua[b] and Yan Jun Liu*[a]

Recent years have witnessed explosive development of chiral plasmonics due to the fact that chiral plasmonic nanostructures give rise to broadband and scalable chiroptical effects orders of magnitude larger than naturally occurring materials. Various chiral plasmonic nanostructures have been demonstrated based on top-down and bottom-up fabrication techniques. However, three-dimensional (3D) chiral plasmonic nanostructure fabrication still remains challenging in many aspects. Here, we demonstrate suspended 3D chiral plasmonic nanostructures fabricated with only one-step electron-beam lithography. Our approach is unique since no alignment is required in the fabrication processes and the top and the bottom structures are self-aligned. Our 3D chiral plasmonic nanostructure consists of a suspended ultrathin silicon nitride membrane with perfectly-aligned L-shape and disk-shape gold nanostructures on its two respective sides. Such suspended chiral plasmonic nanostructures possess strong chiroptical properties at optical frequencies, which can be engineered by simply changing the disk size on one side of the membrane. The origin of the chiroptical properties is also analyzed using the plasmon hybridization model. Experimental results are in good agreement with the finite-difference time-domain simulations. Such suspended chiral plasmonic nanostructures could be highly applicable for chirality analysis of biomolecules, drugs, and chemicals.

Introduction

In recent years, chiral plasmonics or chiroplasmonics, has garnered increasing attention due to the fact that chiral plasmonic nanostructures can produce broadband and scalable chiroptical effects orders of magnitude larger than naturally occurring materials over a broad spectral range.[1,2] Chirally structured plasmonic materials have largely enriched the field of metamaterials with negative refraction,[3,4] and nonlinear optical properties.[5,6] Promising applications have also been demonstrated, such as generation (circular polarizers)[7,8] and detection[9] of circularly polarized light, asymmetric catalysis,[10–12] and chiral recognition and sensing of biomolecules.[13,14]

For chiroptical effects to be clearly observed, the structures should have a chiral length scale that is on the order of or smaller than the wavelength of interest. For many chiral molecules, due to the mismatch of the chiral length scale between light (set by the wavelength of light) and molecules, their chiroptical effects are very weak[15] and hence hardly

detectable. In recent years, researchers have demonstrated that plasmonic structures have extremely strong interaction with circularly polarized light[16] as well as with chiral molecules.[12,13] As a result, the chiroptical effect could be significantly enhanced and be easily detected. In particular, for chiral plasmonic structures exhibiting optical activity in the visible range, they must have nanoscale chiral length. Especially for three-dimensional (3D) chiral nanostructures, they are highly desirable since they can exhibit much stronger chiroptical responses.[17] However, this poses a grand challenge to those fabrication techniques since they have to provide nanoscale-resolution fabrication to match precision and accuracy.

Several strategies have been adopted to achieve chiral nanostructures *via* bottom-up or top-down fabrication techniques. Bottom-up techniques generally refer to chemical synthesis and self-assembly, which offer scalable routes for fabricating chiral structures.[18,19] For examples, surface modified achiral metal nanoparticles with chiral molecules possess noticeable optical activity in the plasmonic resonances of the nanoparticles.[20] Researchers have also successfully demonstrated direct enantioselective synthesis of Au38 nanocluster enantiomers using chiral ligands.[21] Template-directed self-assembly methods seem more appealing for fabricating 3D chiral structures, such as helical superstructures of noble metal nanoparticles assembled by DNA scaffolds,[22–27] cholesteric

[a]*Institute of Materials Research and Engineering, Agency for Science, Technology and Research (A*STAR), 3 Research Link, Singapore 117602, Singapore. E-mail: eunicesp@e.ntu.edu.sg; liuyj@imre.a-star.edu.sg*

[b]*Institute of High Performance Computing, Agency for Science, Technology and Research (A*STAR), 1 Fusionopolis Way, #16-16 Connexis, 138632, Singapore*

liquid crystals,[28] and cellulose nanocrystals,[29,30] respectively. However, the achieved chiroptical effects are generally much weaker than those of structures fabricated using top-down methods due to the lack of accurate control.

In contrast, top-down fabrication usually refers to sophisticated and expensive techniques, which offer high resolution and accuracy. Electron beam lithography (EBL) is a widely used top-down technique that is capable of creating two dimensional arbitrary and complex shapes at the nanometer scale. However, the top-down writing is a planar patterning method, which poses a great challenge for 3D structure fabrication. Although 3D chiral plasmonic nanostructures have been successfully demonstrated using EBL,[31–34] their fabrication requires multiple repeating lithographic steps and additional planarization processes, hence increasing the fabrication complexity and inaccuracy. These repetitions may not only greatly reduce fabrication throughput but also significantly deteriorate the chiroptical performance of the resulting structures due to the inherent inaccuracy in alignment. In addition, from the viewpoint of sensing applications, the planarization layers isolate the direct contacts between chiral plasmonic nanostructures and sensing targets, hence greatly decreasing the sensing sensitivity. Therefore, it is highly desirable to have the chiral plasmonic nanostructures directly exposed without any coverage.

Herein, we present a suspended 3D chiral plasmonic nanostructure using the EBL technique with only one-step electron beam writing process. The 3D chiral plasmonic nanostructure consists of a suspended ultrathin silicon nitride membrane with perfectly-aligned L-shape and disk-shape gold nanostructures on its two respective sides. The suspended membrane provides an ultra-smooth interface and also defines an ultra-uniform gap between the top and bottom layers of gold nanostructures. Our approach is simple and efficient for 3D chiral nanostructures fabrication. Moreover, the coverage issue by the planarization layer is also eliminated in our 3D chiral plasmonic nanostructure. It can be directly exposed to any sensing medium.

Experimental

Chiral plasmonic nanostructures fabrication

Fig. 1(a) shows the schematic view of the fabrication process flow. First, we had a double side polished (100) Si wafer coated with 100 nm thick Si_3N_4 layer grown by low pressure chemical vapor deposition (LPCVD) technique (step 1). The Si wafer was about 250 μm thick and standard photolithography process was carried out on the backside of the wafer to open a 500 μm² square window (step 2). The Si_3N_4 layer was etched with a reactive ion etcher (RIE), (Plasmalab 80plus, Oxford) using a mixture of fluoroform (55 sccm) and oxygen gas (5 sccm) at 55 mTorr chamber pressure and 175 W electric power for ∼3 min to expose the Si wafer (step 3). The wafer was then immersed in potassium hydroxide bath (30 wt%) at 60 °C to etch through Si and leave behind a thin 100 nm thick Si_3N_4 membrane (step 4). The remaining Si_3N_4 layer on the backside of the wafer was then completely etched away by RIE (step 5). The size of the suspended membrane is 150 × 150 μm². A 170 nm thick ZEP-520A
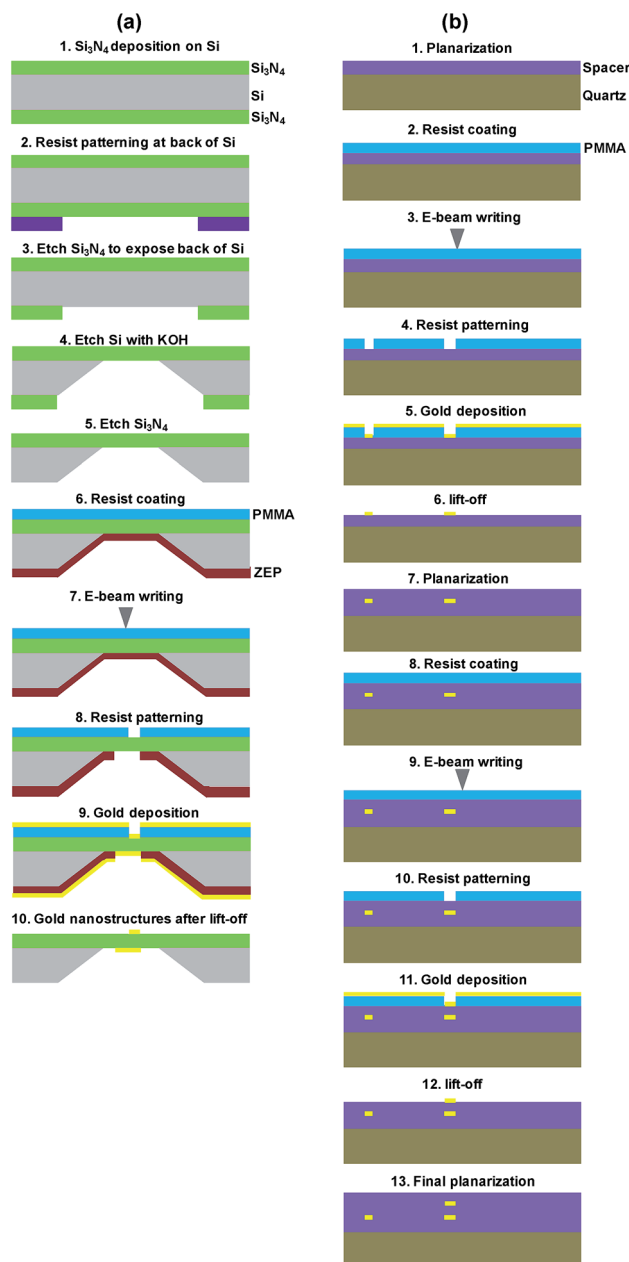

Fig. 1 Schematic of the fabrication process using electron-beam lithography for our (a) and the previously reported (b) 3D chiral plasmonic nanostructures.

(ZEON) resist was spin-coated onto the bottom side of the membrane substrate. The sample was baked at 180 °C for 2 min to remove the solvent in the resists. Then a 200 nm thick polymethyl methacrylate (PMMA) 950A (MicroChem) was spin-coated onto the top side of the Si_3N_4 membrane and the sample was baked at 180 °C for 2 min again (step 6). Designed patterns were exposed by using a focused electron beam with an acceleration voltage of 100 kV and a beam current of 50 pA (ELS-7000, Elionix) (step 7). The exposure doses for the disk and L-shape patterns were 900 μC cm⁻² and 300 μC cm⁻², respectively. The high energy 100 keV electron beam was able to penetrate the top resist layer and Si_3N_4 layer to expose the

resist on the bottom side simultaneously. The exposed samples were developed in Oxylene for 30 s and rinsed in IPA for 20 s (step 8). After resist development, a 2 nm Cr adhesion layer and a 50 nm gold layer were subsequently deposited on both sides of the patterned substrates by an e-beam evaporator (Denton Vacuum, Explorer) at base pressure of 5×10^{-7} Tor and a deposition rate of 0.5 Å s^{-1} (step 9). The lift-off process was carried out by soaking the metal coated samples in Remover 1165 for 30 min (step 10). The samples were then rinsed with acetone, IPA and deionized water and blown dry with nitrogen gas. Fig. 1(b) shows the previously reported fabrication process for a similar structure,[34] which needs more steps and highly accurate alignment (sub-10 nm resolution) technique compared to our method.

Chiroptical characterization

A dark-field (DF) optical microscope (Olympus IX 71) equipped with a spectrometer (Acton SP-2357 Monochromator, Princeton Instruments) was used for the chiroptical characterization, including the optical image and spectrum recording of the samples. A dry DF condenser (NA = 0.8–0.92) was used to focus the incoming circularly polarized white light onto the sample and a 20× objective lens (NA = 0.5) was employed to collect both spectra and DF images through spectrometer and CCD camera respectively. The circular polarization states (either left or right) were generated via a combination of a linear polarizer and a quarter wave plate (working wavelength range: 400–700 nm). Since the collection objective lens has a smaller NA than the dry DF condenser, it only collects a portion of the extinction light signals from the sample.[35] To characterize chiral structures, one normally examines the circular dichroism (CD) spectra. CD refers to the difference in absorbance for left and right circularly polarized light. For our DF configuration, our setup only allows the extinction spectra measurement for circularly polarized light in a limited wavelength range (400–700 nm). Thus we define the extinction difference (ED) of the chiral nanostructures to characterize their chiroptical properties, which is written as $ED = E_{LCP} - E_{RCP}$ with E_{LCP} and E_{RCP} representing the extinction spectra for left and right circularly polarized light respectively.

Numerical simulation

We model the chiroptical properties of the suspended 3D chiral plasmonic nanostructures using the finite-difference time-domain (FDTD) method (Lumerical). Both periodic and perfectly matched layer (PML) boundaries were applied in the x–y plane and z-direction, respectively. A mesh size of 4 nm was set for simulation. The dispersion of gold was based on the Johnson and Christy model in the Lumerical material library.[36] The refractive index of the Si$_3$N$_4$ layer was set to be 2.1 across the interested wavelength range.

Results and discussion

The main idea behind creating 3D plasmonic nanostructures with single-step electron-beam lithography revolves around

distinct sensitivity difference of the selected resists: ZEP and PMMA. Both are high-resolution, positive-tone resists for EBL. In comparison to PMMA, the side groups in ZEP are substituted with a chlorine atom and a phenyl group. ZEP 520A has a molecular weight of 57 000 and is a solution composed of 11% methyl styrene and chloromethyl acrylate copolymer (solid) and 89% anisole (solvent). It has a viscosity of 11 mPa*s and higher sensitivity than PMMA due to the αCl group as well as higher dry etch resistance due to the α-methylstyrene.[37] As the sensitivity of PMMA is much lower than that of ZEP, only the dot patterns exposed in a high dose were well defined in PMMA on the top side. On the bottom side, the L-shape patterns were defined in ZEP with exposure in a low dose. By applying resists of different sensitivities, we achieved different self-aligned patterned shapes on both sides of the membrane.

As a proof of concept, we experimentally tested the sensitivities of the selected resists by exposing them to different electron beam doses. The ZEP and PMMA were spin-coated on Si substrates, respectively. Arrays of $100 \times 100\ \mu m^2$ squares were exposed with various doses (by varying exposure time to get different exposure dose). The exposed samples were then developed in Oxylene for 30 s. We used the surface profiler to measure the step height of square center versus the top resist surface. Then we calculated the sensitivities of ZEP and PMMA by plotting remaining resist thickness versus the exposure dose. Fig. 2 shows the experimentally measured sensitivities of ZEP and PMMA. We can observe a huge difference in sensitivity to the electron-beam exposure between ZEP and PMMA. PMMA shows a much lower sensitivity than ZEP. ZEP can be fully developed at ~200 μC cm^{-2} while PMMA requires ~550 μC cm^{-2} exposure dose of the electron beam, which is more than two times than ZEP does. In addition, ZEP shows much steeper sensitivity slope than PMMA.

With the sensitivity in mind, it is therefore intuitive to arrange the less sensitive PMMA and the more sensitive ZEP layers on the top and bottom of the membrane, respectively. We create an L-disk 3D plasmonic chiral structure by utilizing the sensitivity difference of the ZEP and PMMA resists.
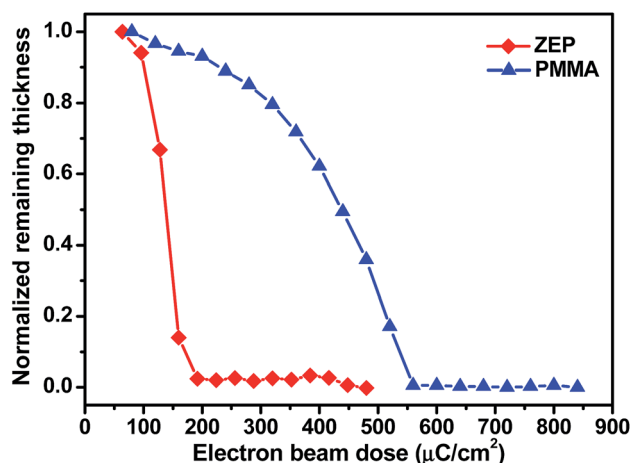

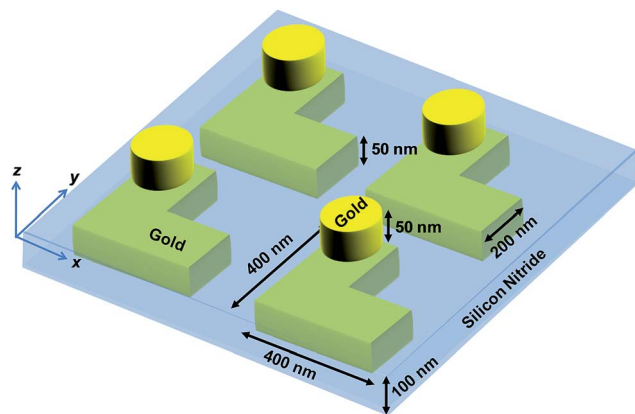Fig. 2 Experimentally measured sensitivities of ZEP and PMMA to the electron beam.

Fig. 3 Schematic view of the designed L-disk plasmonic chiral nanostructures.

Fig. 3 shows a schematic view of the designed L-disk structures. Such a configuration is inspired by the previously reported chiral plasmonic molecules,[34] where the plasmonic molecule is arranged in a C_4 symmetry. Here we simply arrange the L-shape arranged nanoparticles in the same plane into an L-shape nanostructure without changing the C_4 symmetry. The dimension of the L-shape nanostructure is 200 nm in width and 400 nm in length. The period of disk/L-nanostructure arrays at the top/bottom surfaces are 900 nm. For the designed sub-micron sized L-shape on the bottom, exposure dose of 300 µC cm^{-2} was applied to fully develop ZEP patterns, while keeping the PMMA only slightly exposed (keeping >80% remaining thickness). For the disk array on the top, an exposure dose of 900 µC cm^{-2} was applied in order to fully develop PMMA patterns.

Fig. 4(a) shows typical SEM images of the suspended 3D gold nanostructures, where the L-shape gold nanostructures are at the bottom surface of the Si$_3$N$_4$ membrane while the disk-shape ones are at the top surface. Due to the limited depth-of-field of the focused electron beam in SEM, the underneath L-shape gold nanostructures in the SEM image shows a 'blurring' effect. For a clearer view of the L-shape nanostructures, the SEM image was taken directly from the bottom surface, as shown in Fig. 4(b). In our method, the suspended membrane plays a critical role in providing an ultra-smooth interface and uniformly controlled ultra-small gap for fabrication of the top and bottom layers of the nanostructures. The distinguished
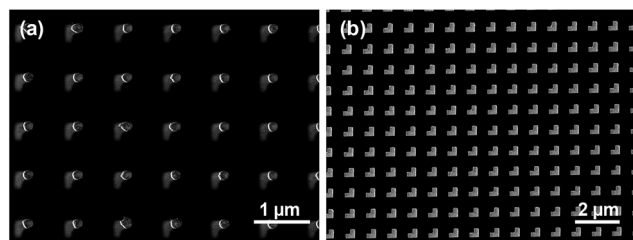
contrast of sensitivity of the selected resists (*i.e.*, PMMA and ZEP) allows us to use different exposure doses of the electron beam to pattern the top and bottom resist layers, respectively. In this way, we are able to create such 3D patterns in single-step electron-beam lithography with self-alignment, hence avoiding the misalignment issue in the multiple lithographic steps. It could also enable us to design the 3D patterns with different symmetries.[38,39]

Another unique point of our fabrication method is that the disk size can be conveniently tuned by varying the designed disk diameters. Fig. 5(a)–(d) shows the disks with gradually reducing size on the top and the L-shape nanostructure with fixed dimensions on the bottom. Fig. 5(e) and (f) shows the measured and simulated ED spectra of the suspended 3D gold chiral nanostructures with the corresponding disk size. Overall, the spectral profiles of simulations and experiments are in good agreement in the wavelength range that our DF microscopy can measure. From Fig. 5(e) and (f), we can clearly see that there are three distinct resonance peaks on the extinction difference (ED) spectra. Compared to the simulation results, the experimentally observed peaks are slightly broadened and blue-shifted. The peak broadening could be caused by the shape tolerance and damping effect of the adhesion layer,[40] while the blue-shift may be due to the positioning tolerance during the fabrication process.

Only plasmon resonances between the top and bottom nanostructure layers take place at similar frequencies and they are efficiently coupled, exhibiting strong chiroptical responses. This can be proven by changing the disk size at the top layer. Reducing the diameter of the disks in Fig. 5 from 190 to 120 nm significantly weakens the coupling strength between the top and bottom layers as we can see that the resonance peaks become weak with a decreasing disk size. It is therefore expected that the chiroptical response will diminish significantly at a sufficiently reduced size of the disks. In this case, the resonance frequencies of the top and bottom nanostructure layers will be too different to facilitate an efficient coupling. As a result, such a system cannot exhibit a chiral optical
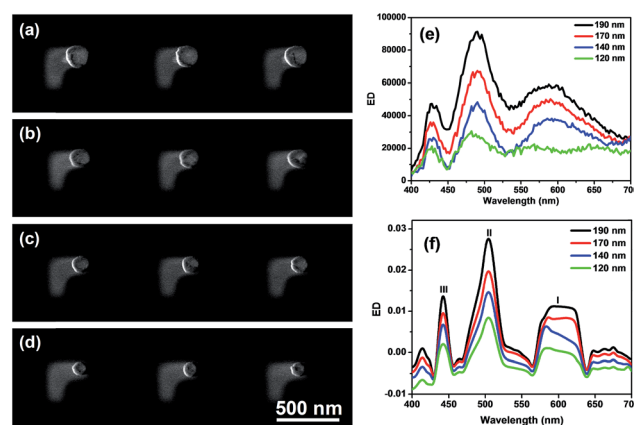

Fig. 4 Typical SEM images of the suspended 3D gold nanostructures (a) top-view of the disk-array and (b) bottom-view of the L-array.

Fig. 5 Suspended 3D gold nanostructures with varying size of the disk (a) *d* = 190 nm, (b) *d* = 170 nm, (c) *d* = 140 nm, and (d) *d* = 120 nm. Measured (e) and simulated (f) ED spectra of the suspended 3D gold chiral nanostructures with varying disk size.

response even though the system still physically shows a structural handedness.

To further probe the origin of these modes, we decompose the L-disk structures into the isolated L-shape and disk arrays based on the plasmon hybridization model.[41–43] The extinction spectra of isolated L-shape and disk arrays were simulated and their near-field electric-field and charge distributions were also calculated at their extinction peaks (Fig. 6 and 7). Clearly, we can observe localized surface plasmon resonances (LSPR) from each of them. For the disk arrays, there is a broad resonance across our measured wavelength range (400–700 nm) with the peak intensity and linewidth dependent on the disk size [Fig. 6(a)]. The electric field and charge distributions [Fig. 6(b) and (c)] show that the broad resonance results from the dipole plasmon mode of the disks. While for the L-shape array, there are two LSPR resonance modes that locate at 440 nm and 600 nm, respectively, within our interested wavelength range [Fig. 7(a) and (d)]. The charge distributions [Fig. 7(c) and (f)] show that the resonance at 600 nm results from the dipolar plasmon resonance mode, while the resonance at 440 nm comes from the quadrupolar plasmon resonance mode. When we put these separated structures together, the plasmon mode hybridization happens. As a result, we observed three main resonance modes in the L-disk structures. From the above analysis, we can therefore ascribe the observed modes I and III to the dipole–dipole, dipole–quadrupole couplings between L-shape and disk structures. As for mode II, it is obvious that the dipole resonance from the disk plays a dominant role. However, both dipole and quadrupole resonance from L-shape structure will also contribute partially, hence making the resonance of mode II slightly complex. It is worth mentioning that in the previously reported chiral plasmonic molecules,[34] the L-shape arranged isolated nanoparticles in the same plane can only give rise to the dipole plasmonic resonance; while in our design, the L-shape nanostructure can produce the quadrupole resonance. In general, the high-order plasmon modes have a narrower spectral resonance than the low-order ones.[44] Our experimental and simulation results have also confirmed that the dipole–quadrupole hybridized mode (mode III) has a much higher Q factor (mode III, Q: ~17)

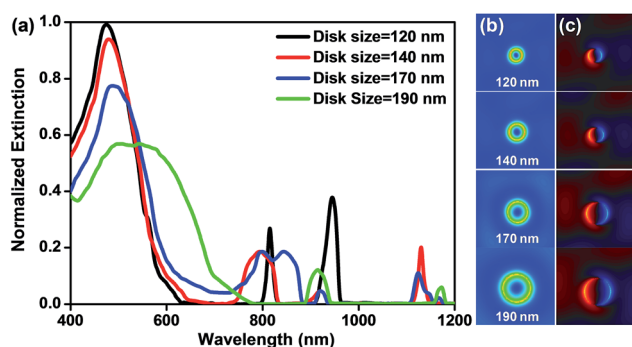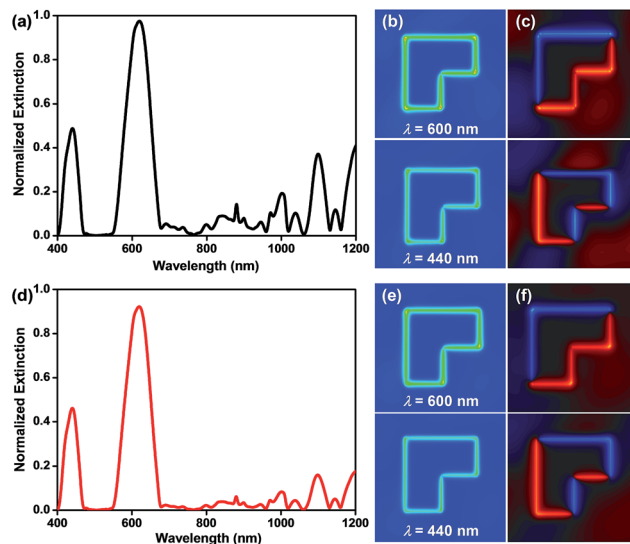Fig. 7 Simulated extinction spectra for both left- (a) and right-handed (d) circularly polarized light of the isolated L-shape array on the Si_3N_4 membrane. Corresponding electric field (column b and e) and charge (column c and f) distributions of the L-shape arrays at the extinction peaks of 600 nm and 440 nm, respectively.

than the dipole–dipole one (mode I, Q: 7.5). This narrow spectral resonance with high Q factor is particularly beneficial to sensing applications since it could provide high sensitivity.

Conclusions

In summary, we have demonstrated a suspended 3D chiral plasmonic nanostructure using only one-step electron-beam lithography. No alignment process is involved and the top and the bottom nanostructures are self-aligned, thus avoiding misalignments inherent with multiple lithographic steps. The suspended 3D chiral plasmonic nanostructures have also exhibited very strong chiroptical properties, which are potentially useful for chirality analysis of biomolecules, drugs, and chemicals. Compared to the 2D planar structures,[13] the 3D structures could greatly increase the adsorption areas of the molecules. More importantly, our 3D chiral plasmonic nanostructures can also create narrow spectral resonances due to the higher-order plasmon resonances. These will significantly enhance the detection sensitivity of biospectroscopies/biosensors that utilize the suspended 3D structures.

Acknowledgements

Notes and references

1 A. Guerrero-Martínez, J. L. Alonso-Gómez, B. Auguié, M. M. Cid and L. M. Liz-Marzán, *Nano Today*, 2011, **6**, 381.

Fig. 6 (a) Simulated extinction spectra of the isolated disk array on the Si_3N_4 membrane for left-handed circularly polarized light. Electric field (column b) and charge (column c) distributions of the disk arrays at the extinction peak of ~500 nm.

2   V. K. Valev, J. J. Baumberg, C. Sibilia and T. Verbiest, *Adv. Mater.*, 2013, **25**, 2517.

3   J. B. Pendry, *Science*, 2004, **306**, 1353.

4   S. Zhang, Y. S. Park, J. S. Li, X. C. Lu, W. L. Zhang and X. Zhang, *Phys. Rev. Lett.*, 2009, **102**, 023901.

5   M. Kauranen and A. V. Zayats, *Nat. Photonics*, 2012, **6**, 737.

6   S. P. Rodrigues, S. Lan, L. Kang, Y. Cui and W. Cai, *Adv. Mater.*, 2014, **26**, 6157.

7   J. K. Gansel, M. Thiel, M. S. Rill, M. Decker, K. Bade, V. Saile, G. von Freymann, S. Linden and M. Wegener, *Science*, 2009, **325**, 1513.

8   Y. Zhao, M. A. Belkin and A. Alù, *Nat. Commun.*, 2012, **3**, 870.

9   I. Hodgkinson and Q. H. Wu, *Adv. Mater.*, 2001, **13**, 889.

10 M. Tamura and H. Fujihara, *J. Am. Chem. Soc.*, 2003, **125**, 15742.

11 A. S. K. Hashmi and G. J. Hutchings, *Angew. Chem., Int. Ed.*, 2006, **45**, 7896.

12 Y. Tang and A. E. Cohen, *Science*, 2011, **332**, 333.

13 E. Hendry, T. Carpy, J. Johnston, M. Popland, R. V. Mikhaylovskiy, A. J. Lapthorn, S. M. Kelly, L. D. Barron, N. Gadegaard and M. Kadodwala, *Nat. Nanotechnol.*, 2010, **5**, 783.

14 X. Wu, L. Xu, L. Liu, W. Ma, H. Yin, H. Kuang, L. Wang, C. Xu and N. A. Kotov, *J. Am. Chem. Soc.*, 2013, **135**, 18629.

15 N. Berova, K. Nakanishi and R. Woody, *Circular Dichroism: Principles and Applications*, Wiley, New York, 2000.

16 A. Papakostas, A. Potts, D. M. Bagnall, S. L. Prosvirnin, H. J. Coles and N. I. Zheludev, *Phys. Rev. Lett.*, 2003, **90**, 107404.

17 C. M. Soukoulis and M. Wegener, *Nat. Photonics*, 2011, **5**, 523.

18 A. Guerrero-Martínez, J. L. Alonso-Gómez, B. Auguié, M. M. Cid and L. M. Liz-Marzán, *Nano Today*, 2011, **6**, 381.

19 A. Ben-Moshe, B. M. Maoz, A. O. Govorov and G. Markovich, *Chem. Soc. Rev.*, 2013, **42**, 7028.

20 A. O. Govorov, Z. Fan, P. Hernandez, J. M. Slocik and R. R. Naik, *Nano Lett.*, 2010, **10**, 1374.

21 Q. Xu, S. Kumar, S. Jin, H. Qian, M. Zhu and R. Jin, *Small*, 2014, **10**, 1008.

22 A. Guerrero-Martínez, B. Auguié, J. L. Alonso-Gómez, Z. Džolić, S. Gómez-Graña, M. Žinić, M. M. Cid and L. M. Liz-Marzán, *Angew. Chem., Int. Ed.*, 2011, **50**, 5499.

23 G. Shemer, O. Krichevski, G. Markovich, T. Molotsky, I. Lubitz and A. B. Kotlyar, *J. Am. Chem. Soc.*, 2006, **128**, 11006.

24 J. Sharma, R. Chhabra, A. Cheng, J. Brownell, Y. Liu and H. Yan, *Science*, 2009, **323**, 112.

25 X. Shen, C. Song, J. Wang, D. Shi, Z. Wang, N. Liu and B. Ding, *J. Am. Chem. Soc.*, 2012, **134**, 146.

26 A. Kuzyk, R. Schreiber, Z. Fan, G. Pardatscher, E.-M. Roller, A. Högele, F. C. Simmel, A. O. Govorov and T. Liedl, *Nature*, 2012, **483**, 311.

27 R. Schreiber, N. Luong, Z. Fan, A. Kuzyk, P. C. Nickels, T. Zhang, D. M. Smith, B. Yurke, W. Kuang, A. O. Govorov and T. Liedl, *Nat. Commun.*, 2013, **4**, 2948.

28 R. Bitar, G. Agez and M. Mitov, *Soft Matter*, 2011, **7**, 8198.

29 H. Qi, K. E. Shopsowitz, W. Y. Hamad and M. J. MacLachlan, *J. Am. Chem. Soc.*, 2011, **133**, 3728.

30 A. Querejeta-Fernandez, G. Chauve, M. Methot, J. Bouchard and E. Kumacheva, *J. Am. Chem. Soc.*, 2014, **136**, 4788.

31 M. Decker, M. Ruther, C. E. Kriegler, J. Zhou, C. M. Soukoulis, S. Linden and M. Wegener, *Opt. Lett.*, 2009, **34**, 2501.

32 C. Helgert, E. Pshenay-Severin, M. Falkner, C. Menzel, C. Rockstuhl, E.-B. Kley, A. Tünnermann, F. Lederer and T. Pertsch, *Nano Lett.*, 2011, **11**, 4400.

33 C. Menzel, C. Helgert, C. Rockstuhl, E.-B. Kley, A. Tünnermann, T. Pertsch and F. Lederer, *Phys. Rev. Lett.*, 2010, **104**, 253902.

34 M. Hentschel, M. Schaferling, T. Weiss, N. Liu and H. Giessen, *Nano Lett.*, 2012, **12**, 2542.

35 R. Mercatelli, G. Romano, F. Ratto, P. Matteini, S. Centi, F. Cialdai, M. Monici, R. Pini and F. Fusi, *Appl. Phys. Lett.*, 2011, **99**, 131113.

36 P. B. Johnson and R. W. Christy, *Phys. Rev. B: Solid State*, 1972, **6**, 4370.

37 K. Koshelev, M. A. Mohammad, T. Fito, K. L. Westra, S. K. Dew and M. Stepanova, *J. Vac. Sci. Technol., B: Nanotechnol. Microelectron.: Mater., Process., Meas., Phenom.*, 2011, **29**, 06F306.

38 S. M. Barlow and R. Raval, *Surf. Sci. Rep.*, 2003, **50**, 201.

39 Z. Fan and A. O. Govorov, *Nano Lett.*, 2010, **10**, 2580.

40 T. G. Habteyes, S. Dhuey, E. Wood, D. Gargas, S. Cabrini, P. J. Schuck, A. P. Alivisatos and S. R. Leone, *ACS Nano*, 2012, **6**, 5702.

41 E. Prodan, C. Radloff, N. J. Halas and P. Nordlander, *Science*, 2003, **302**, 419.

42 H. Liu, E. S. P. Leong, Z. Wang, G. Si, L. Zheng, Y. J. Liu and C. Soci, *Adv. Opt. Mater.*, 2013, **1**, 978.

43 H. Liu, Z. Wang, J. Huang, Y. J. Liu, H. J. Fan, N. I. Zheludev and C. Soci, *Nano Lett.*, 2014, **14**, 5162.

44 B. Luk'yanchuk, N. I. Zheludev, S. A. Maier, N. J. Halas, P. Nordlander, H. Giessen and C. T. Chong, *Nat. Mater.*, 2010, **9**, 707.